ADVANCED FUNCTIONAL MATERIALS
www.afm-journal.de

Design and Assembly of Continuous Macro-Micro-Porous Metal-Organic Framework Film Assisted by Atomic Layer Deposition for Biosensing

Jinlong Wang, Yuanyuan Jiang, Fenyang Zhu, Yu Mei, Zhiyuan Qiao, Zhe Zhao, Zhi Zheng, Zihan Lu, Xuanyong Liu, Yongfeng Mei, and Gaoshan Huang**

Constructing highly oriented and ordered macro-pores on metal-organic framework (MOF) film can surpass the inherent limitations from micro-pores, promote multiphase adsorption, and expedite electrochemical reaction, but the fabrication remains extremely challenging. Here, continuous macro-micro-porous MOF films are achieved by combining polystyrene microsphere template and induction effect of ZnO nanomembrane prepared by atomic layer deposition. In addition to the intrinsic micro-pores, the fabricated MOF film exhibits oriented and ordered macro-porous structures. Compared with the macro-porous MOF particles and conventional MOF film, the mass diffusion and charge transportation in the macro-micro-porous MOF film are significantly improved, endowing the film with excellent electrochemical activity. The sensor device made from macro-micro-porous ZIF-67 film toward glucose exhibits excellent performance, e.g., high sensitivity, low limit of detection, and fast response, due to rapid glucose molecule diffusion and enhanced exposure of active sites via interconnected macro-porous channels. This work paves the way for the application of MOF film in high-performance biosensor chip and therefore may have great potential in post-Moore period.

1. Introduction

Porous materials are widely utilized in various research fields such as gas separation, chemical catalysis, and biosensing.[1–3] Particularly, crystalline network materials possessing uniform micro-pore structure (<2 nm), including metal-organic frameworks (MOF), hydrogen bond organic frameworks (HOF), and covalent organic frameworks (COF), etc.,[4–6] exhibit exceptional catalytic and sensing capabilities due to their tunable pore diameter and uniform diameter distribution.[7] However, the intrinsic pore size of these materials (represented by MOF), typically concentrates on the micro-pore range.[8] Such small pores inevitably impede the permeation of molecules, which results in restricted diffusion of the reactants/products in catalytic reactions, thereby hindering performance enhancement.[9] Preserving the original micro-pores of the crystal and introducing macro-pores to fabricate a hierarchically macro-micro-porous structure are effective strategies to overcome the limitations of micro-pores, achieving fast mass diffusion and full exposure of active sites.[10] The synthesis strategies for constructing hierarchically porous systems on the basis of micro-porous crystals primarily encompass template-assisted synthesis, defect-induced method, acid-base etching, etc.[11–13] Among them, the template-assisted synthesis is considered as the most efficient and convenient approach for synthesizing highly ordered

J. Wang, F. Zhu, Y. Mei, Z. Qiao, Z. Zheng, Y. Mei, G. Huang
Department of Materials Science
International Institute of Intelligent Nanorobots and Nanosystems
State Key Laboratory of Surface Physics
State Key Laboratory of Photovoltaic Science and Technology
Fudan University
Shanghai 200438, P. R. China
E-mail: gshuang@fudan.edu.cn

Z. Zhao, X. Liu
State Key Laboratory for Modification of Chemical Fibers and Polymer Materials
College of Biological Science and Medical Engineering
Donghua University
Shanghai 201620, P. R. China
E-mail: zhezhao@dhu.edu.cn

The ORCID identification number(s) for the author(s) of this article can be found under https://doi.org/10.1002/adfm.202419775

DOI: 10.1002/adfm.202419775

J. Wang, F. Zhu, Y. Mei, Z. Qiao, Z. Zheng, Y. Mei, G. Huang
Yiwu Research Institute of Fudan University
Yiwu, Zhejiang 322000, P. R. China

Y. Jiang
Key Laboratory of Materials Physics
Institute of Solid State Physics
HFIPS
Chinese Academy of Sciences
Hefei 230031, P. R. China

Y. Mei
Shanghai Frontiers Science Research Base of Intelligent Optoelectronics and Perception
Institute of Optoelectronics
Fudan University
Shanghai 200438, P. R. China

Y. Jiang
University of Science and Technology of China
Hefei 230026, P. R. China

macro-micro-porous structures.[14] The typical template-assisted method involves growing micro-porous crystals in the empty spaces of 3D ordered polymer templates, followed by removal of the template to obtained an ordered hierarchically porous structure.[15] The ordered macro-pores channels facilitate rapid diffusion of substances in MOFs, significantly enhancing the performance of electrocatalytic reactions and the recyclability in bulky-molecule reactions.[16]

Recently, the obtained MOF crystals with macro-micro-porous via the template method were used to promote the catalytic reactions including benzaldehyde conversion, CO_2 conversion, aluminum-ion batteries, and hydrogen evolution reaction.[17–20] Notably, the rigid crystal particles can result in an unstable electronic conduction network and uncontrollable crystal distribution, leading to performance degradation.[21] Additionally, dispersed crystal particles are difficult to be effectively applied into integrated devices, greatly limiting the application of macro-micro-porous MOF structures.[22] It is worth noting that the assembly of macro-micro-porous MOF particles into film form may effectively address these issues.[23] Previous investigation demonstrates that film composed of assembled crystal particles possesses a stable charge transportation, uniformly distributed crystals, and fully exposed active sites.[24,25] Thus it is reasonable to deduce that porous materials in film form should possess superior performance compared to their counterpart in particle form.[26] However, up to now, there is no hierarchically porous MOF film with intentionally introduced macro-pores that has been realized. During the fabrication process, the harsh experimental conditions can easily cause decomposition of the polymer template, making it problematical to assemble crystal particles into dense films.[27] Moreover, the structural support force of the macro-porous film itself is insufficient to offset the surface tension of liquids, resulting in structural collapse.[28] Based on these premises, it is highly necessary to develop reliable methods for designing and fabricating macro-micro-porous film with oriented and ordered structure.

Here, we present a synthesis strategy for fabricating continuous MOF film with ordered macro-micro-porosity, by using ZIF-67 as a proof of concept. Specifically, a ZnO nanomembrane is deposited as an inducing layer by atomic layer deposition (ALD) on the surface of 3D ordered polystyrene sphere (PS) template. When saturated precursor solution fills into the empty space of the template, MOF is crystallized under the induction of the ZnO nanomembrane to form a uniform and dense film. After removing the template by organic solvent, a MOF film with an ordered hierarchically macro-micro-porous structure is formed, and critical point drying (CPD) is used to resolve the structural collapse dilemma during the drying process. Currently, we integrate the obtained ordered macro-micro-porous ZIF-67 film (OMMF-ZIF-67) with flexible device to prepare a skin sweat glucose sensor, and it exhibits an ultrahigh sensitivity of 5280 $\mu A\ mM^{-1}\ cm^{-2}$, far exceeding those of the macro-micro-porous ZIF-67 crystals (MMC-ZIF-67) and the normal ZIF-67 film. We believe that this fabrication strategy can provide new insights into the functional film assembly of hierarchically porous materials and promote their application in electrochemistry-related fields.

2. Results and Discussion

Figure 1a shows the schematic diagrams of the fabrication process for ordered macro-micro-porous MOF film (OMMF-MOF). First, monodisperse PS with a sphere size of ≈200 nm are initially assembled into a 3D ordered PS template (Figure S1, Supporting Information). Subsequently, ZnO nanomembrane is deposited onto all the surface of the PS template by ALD (denoted as ALD-ZnO@PS) as an inducing layer. The PS template is then immersed in a specific precursor saturated solution for MOF nucleation and crystallization (the precursor solution for OMMF-ZIF-67 is a saturated methanol solution of cobalt nitrate and 2-methylimidazole), and MOF crystallizes within the empty space of the PS template due to the induction effect of ZnO nanomembrane. The detailed growth mechanism of assembly of the MOF film has been elucidated in our previous investigation.[29] As the last step, the PS template is removed in dimethylformamide, yielding an MOF film with ordered macro-micro-porous structure, and its thickness is basically in accordance with that of the PS template. It should be noted that CPD process is required here for OMMF-MOF, otherwise, the macro-porous structure within the film will collapse (Figure S2, Supporting Information). The morphologies of the samples in each step are illustrated by field-emission scanning electron microscopy (FESEM) images in Figure 1a. The high-resolution structural model of OMMF-MOF is illustrated in Figure 1b, and the confinement effect of the PS template causes the building units of MOF to crystallize in an orderly manner on the outer surface of the PS to form ordered macro-pores (Figure 1c). Moreover, the crystal building units of the MOF have a unique network structure itself through coordination polymerization,[30] creating an abundance of micro-pores (Figure 1d), thereby forming a hierarchically macro-micro-porous structure. The pore characteristics of OMMF-MOF are validated through nitrogen adsorption-desorption experiments and mercury intrusion porosimetry tests, and the results are depicted in Figure 1e. One can see that the sample exhibits a wealth of micro-pores with an average diameter of ≈0.6 nm and macro-pores of ≈100 nm, and this causes the formation of channels through neighboring macro-pores inside the macro-micro-porous film.[17]

The removal of the PS template enables OMMF-MOF to be free-standing in solution, facilitating the transfer and application of the MOF film. The prepared free-standing OMMF-ZIF-67 can be integrated to the sensing region of a flexible sensor to set up an epidermal sweat sensing device, and the flexible sensing device exhibits significant fitting ability on human skin (Figure 1f). As shown in the structural diagram of the sensing device in Figure 1f, a single sensing device includes a flexible and mechanically robust polydimethylsiloxane (PDMS) substrate, a patterned Cr/Au layer for signal transmission, an OMMF-ZIF-67 sensing layer serving as the working electrode, a Ag/AgCl layer serving as the reference electrode, and an encapsulation layer promoting the long-term usage and anti-disturbance property in sweat analysis of the device. The detailed preparation process of the epidermal sweat sensing device is shown in Figure S3 (Supporting Information). Considering the direct contact of the sensing

Z. Lu
Shanghai Center of Biomedicine Development
Shanghai 201203, P. R. China

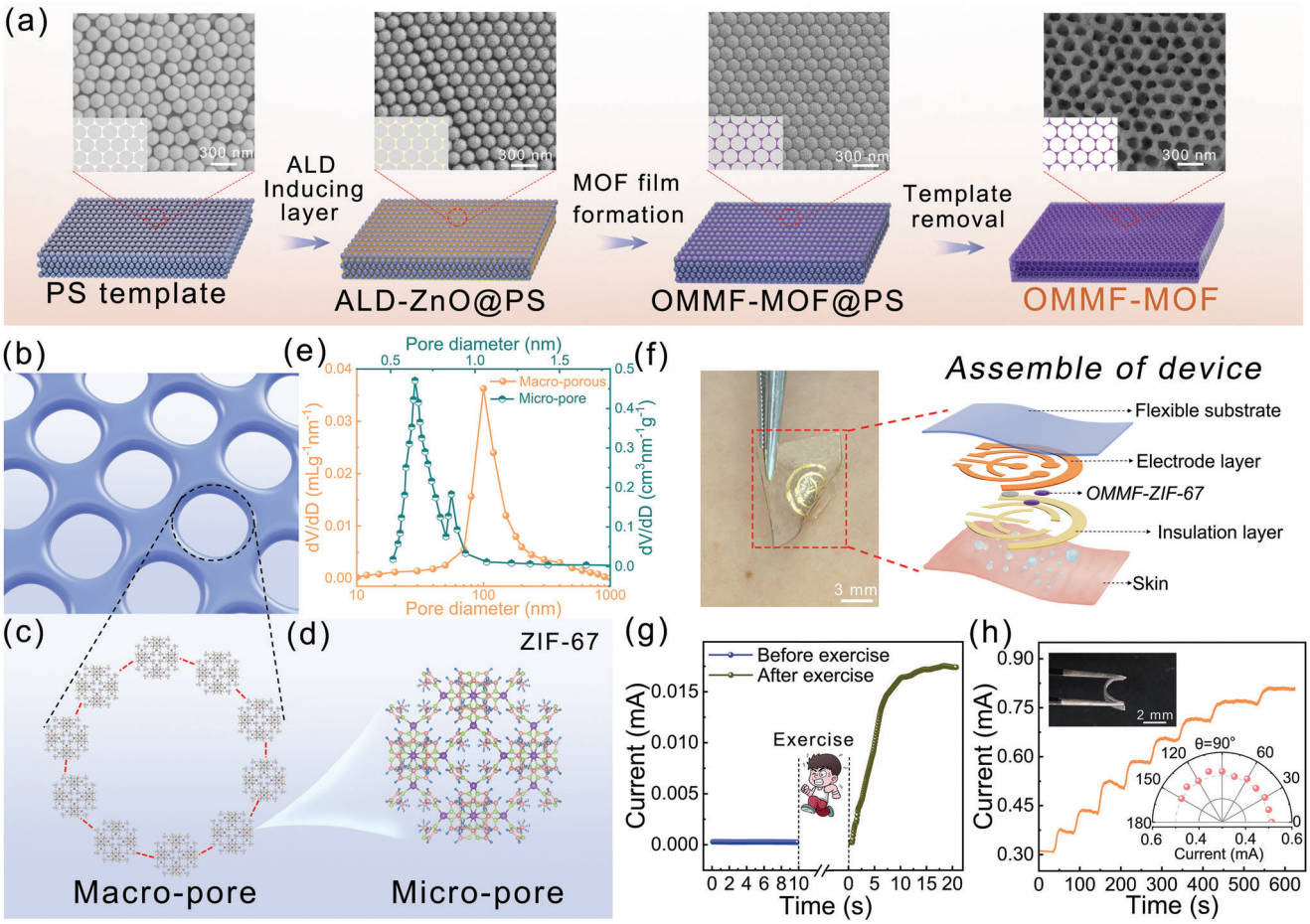

Figure 1. a) Schematics of the preparation process of OMMF-MOF and FESEM images of the corresponding samples, with insets illustrating top view schematics. b) Structural model of OMMF-MOF. c) Molecular model of the mechanism of macro-pores formation. d) Model of MOF building units. e) Pore size distribution of micro- and macro-pores of OMMF-ZIF-67. f) Photograph of a wearable epidermal sweat sensing device made from OMMF-ZIF-67 and layered configuration of the device. g) Sweat glucose sensing results of the epidermal sweat sensor on experimenter before and after exercise. h) Current response to repeatedly added 0.1 mM glucose, and OMMF-ZIF-67 sensor was tested in bent state after 50 bending cycles. The upper-left inset shows the photo of a 120° bent sensor. The lower-right inset shows the responses of the flexible sensor device toward 1 mM glucose measured at different bending angles.

device with human skin, a biocompatibility study of the OMMF-ZIF-67 was investigated using human dermal fibroblasts. In the experiment, human dermal fibroblasts were co-cultured with OMMF-ZIF-67 extract for three days, and the fluorescence staining results indicate that cells cultured with OMMF-ZIF-67 exhibit homogeneous size and regular morphology, and no significant cell apoptosis is observed (Figure S4a, Supporting Information). Furthermore, the cell counting statistical comparison results in Figure S4b (Supporting Information) also confirmed the biological safety of the OMMF-ZIF-67 for epidermal sweat sensing applications. Figure 1g illustrates the analytical capability of the sensing device for sweat glucose. The sensing current of the device attached to the experimenter's epidermis after exercise shows significant changes compared to that before exercise. In addition, the device maintains a linear and highly sensitive response to glucose after repeated bending deformation (Figure 1h and its upper-left inset), showing no significant change in current (Figure S5, Supporting Information). The lower-right inset of Figure 1h elucidates that the sensor at various bending angles demonstrates consistent response currents toward glucose molecules. The results confirm that the sensing device possesses glucose sensing capability to actual sweat and mechanical integrity against the expected deformation of the wearer's daily activities.

The FESEM image of OMMF-ZIF-67 in **Figure 2**a and corresponding energy dispersive X-ray spectroscopy (EDX) spectrum in Figure S6 (Supporting Information) demonstrate the surface morphology and composition of the sample. It is noted that the macro-pores are tightly and orderly arrayed on the surface and inner part of the film (Figure S7, Supporting Information). For comparison, MMC-ZIF-67 was prepared by using the fabrication process reported in literature (Figure S8a, Supporting Information),[17] which demonstrates particle format after the PS template is removed as there is no inducing effect of ZnO nanomembrane on the surface of PS template (Figure S9, Supporting Information). FESEM images of MMC-ZIF-67 (Figure 2b) displayed a decahedral morphology of ZIF-67 crystal particles with ordered macro-pores. Compare with

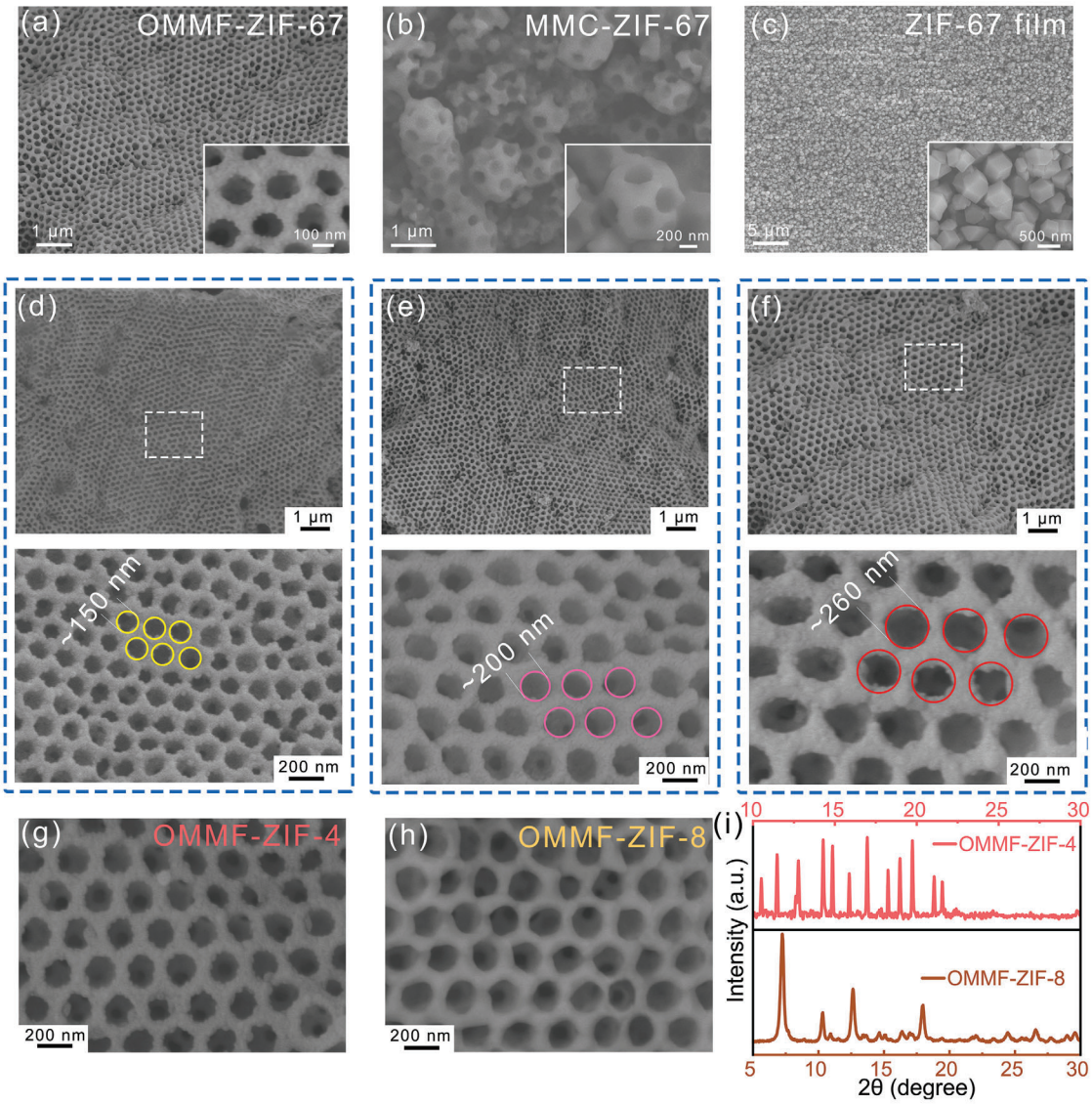

Figure 2. FESEM images with different magnifications of a) OMMF-ZIF-67, b) MMC-ZIF-67, and c) ZIF-67 film. FESEM images of OMMF-ZIF-67 with different sizes of macro-pores achieved by modulating PS size: d) ≈150 nm, e) ≈200 nm, and f) ≈260 nm. The bottom images are enlarged views of the areas outlined by the boxes in top images. FESEM images of OMMF-MOF formed by different MOFs: g) ZIF-4 and h) ZIF-8. i) XRD spectra corresponding to OMMF-ZIF-4 and OMMF-ZIF-8.

OMMF-ZIF-67, the MMC-ZIF-67 are rigidly and independently distributed, which may result in discontinuity in the electron conduction network, thereby affecting electrochemical performance.[22] The conductivity test results confirm that the continuous film state possesses a higher conductivity (Figure S10, Supporting Information). A ZIF-67 film induced by the ZnO nanomembrane without macro-pores is also prepared as a reference (Figure S8b, Supporting Information), which exhibits a uniform distribution of film state structure (Figure 2c), but lacks specifically designed macro-pores. In addition, Figure S11 (Supporting Information) exhibits the statistics of the macro-pore size in OMMF-ZIF-67 and a uniform size distribution is noticeable. Since the macro-pore size is determined by the diameter of the PS, experimentally, we engineered PS template with sphere diameters ranging from ≈150 to ≈260 nm and assembled ZIF-67 film with the inducing effect of ZnO nanomembrane. The confinement effect of the PS template during the synthesis of OMMF-ZIF-67 was observed in all the samples, and this led to uniform macro-pores with sizes correspond to those of previous PS microspheres, thereby producing a series of OMMF-ZIF-67 samples with macro-pore sizes ranging from ≈150 to ≈260 nm. Here, stable, dense, homogeneous, and crack-free OMMF-ZIF-67 with different macro-pores are clearly observed in magnified FESEM images (Figure 2d–f). Moreover, it is worth noting that the current approach not only enables the synthesis of ZIF-67-based structure but also can be applied to other macro-microporous MOF films through altering the precursor solution, and MOFs like ZIF-4, ZIF-8, etc. has been prepared (Figure 2g,h).

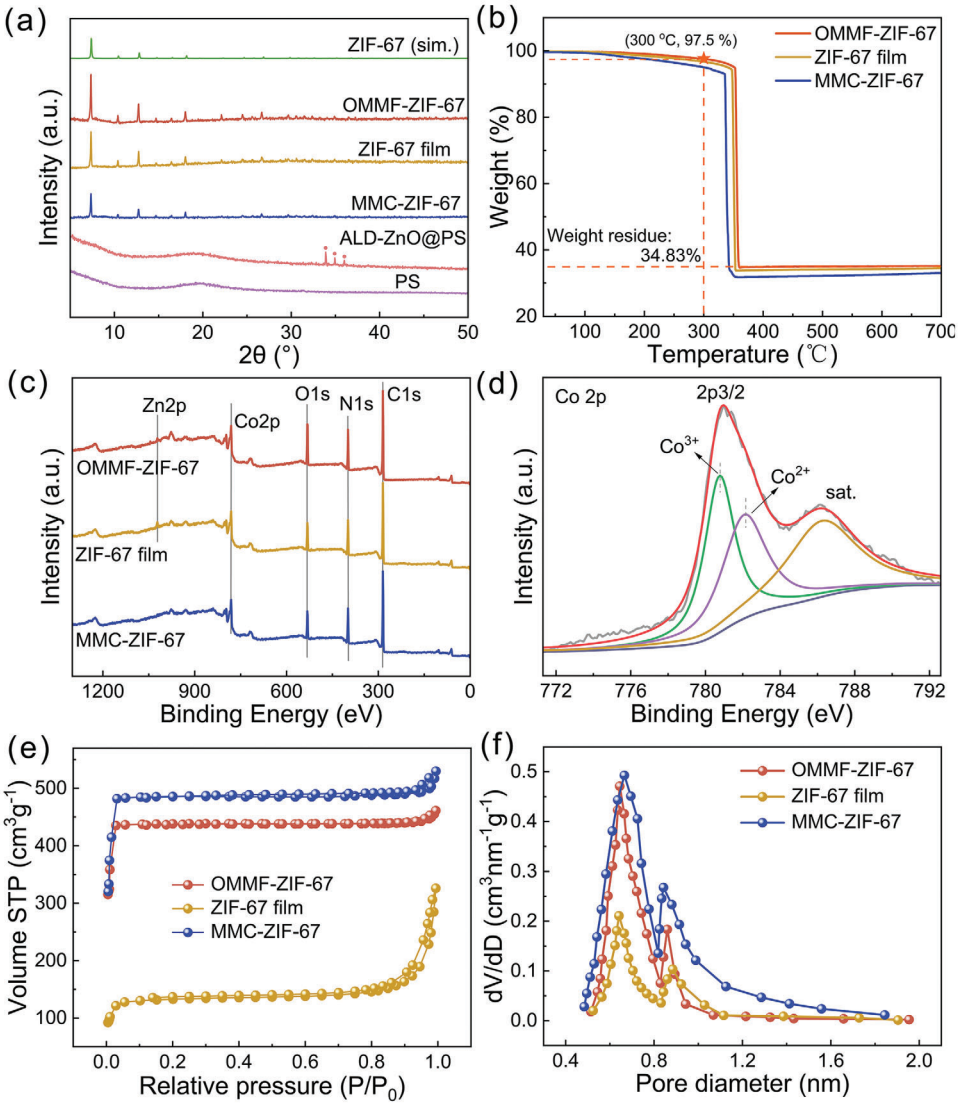

Figure 3. a) XRD patterns of PS template, ALD-ZnO@PS, ZIF-67 film, MMC-ZIF-67, and OMMF-ZIF-67. The solid circles indicate the peaks from ZnO crystals. b) TGA curves of OMMF-ZIF-67, ZIF-67 films, and MMC-ZIF-67. c) XPS survey scans of OMMF-ZIF-67, ZIF-67 film, and MMC-ZIF-67. d) High resolution Co $2p_{3/2}$ spectrum of OMMF-ZIF-67. e) Nitrogen adsorption-desorption isotherms of OMMF-ZIF-67, ZIF-67 film, and MMC-ZIF-67. f) Pore size distribution of OMMF-ZIF-67, ZIF-67 film, and MMC-ZIF-67.

The confinement effect of the PS template results in similar continuous macro-micro-porous film morphologies, rather than the growth of crystal shapes (such as the elongated shape of ZIF-4 film illustrated in Figure S12, Supporting Information). The X-ray diffraction (XRD) spectra in Figure 2i verifies that OMMF-MOF samples grown by current approach still maintain a high degree of crystallinity. These results confirm the general applicability of the proposed templating method for macro-pore formation and strategy of ALD-assisted fabrication of continuous macro-micro-porous MOF film.

In current work, the crystal structures of OMMF-ZIF-67 and related samples are studied in detail, as shown in **Figure** 3a. The broad peak of the PS template located around ≈20° is attributed to the amorphous structure of organics.[31] After depositing ZnO nanomembrane by ALD, the diffraction peaks associated with the (100), (002), and (101) lattice planes of wurtzite ZnO are observed (indicated by the solid circles in Figure 3a), proving the co-existence of amorphous organic and polycrystalline ZnO.[32] For three different structures of ZIF-67, all diffraction peaks conform well to the simulated spectrum, which confirms the formation of highly crystalline ZIF-67. These experimental results indicate that irrespective of ZIF-67′s form, be it particle or film, and regardless of the presence of macro-micro-pores within the film, the crystal structure of the MOF remains consistent. Since temperature has a significant impact on the stability of crystal structures, thermal gravimetric analysis (TGA) is performed to assess the thermal stabilities of the samples. As illustrated in Figure 3b, at 300 °C, the mass decrease for OMMF-ZIF-67 is ≈2.5% only. Significant mass decrease is negligible until the temperature rises to 350 °C, which is attributed to the oxidative degradation

of the organic linker.[33] Notably, the degradation temperature of ZIF-67 in film form is relatively higher than that in particle form (≈12 °C). This may be ascribed to the protective effect of the residual inducing layer (i.e., ZnO nanomembrane) which enhances the thermal stability of the structure.[34] Further investigation of the elemental and chemical states of three ZIF-67-based structures is conducted by X-ray photoelectron spectroscopy (XPS). The XPS spectrum of MMC-ZIF-67 reveals the presence of Co, C, N, and O, while spectra of OMMF-ZIF-67 and ZIF-67 films indicate the presence of Co, C, N, O, and residual Zn (Figure 3c), due to incomplete conversion of inducing ALD ZnO nanomembrane. In addition, the intensities of peaks from other elements remain essentially unchanged, indicating that the macro-micro-porous structure do not affect the chemical state of the ZIF-67. Moreover, the high-resolution Co $2p_{3/2}$ spectrum of OMMF-ZIF-67 can be deconvolved into three peaks at ~780.8, ~782.2, and ~786.4 eV, corresponding to Co^{3+}, Co^{2+}, and satellite species,[29] respectively (Figure 3d), which will be utilized for following electrochemical sensing. The high-resolution C 1s, O 1s, and N 1s spectra of OMMF-ZIF-67 are illustrated in Figure S13 (Supporting Information), where the C—C and C—N bonds from the imidazole ring within the crystal structure are obvious.[35] For the XPS spectrum of N 1s, the coexistence of C═N and oxygen-N peaks indicates the substitution of H atoms by O atoms adjacent to N atoms.[36] Further nitrogen adsorption-desorption experiments were conducted to investigate the porosity of the samples, and the results are shown in Figure 3e. OMMF-ZIF-67, MMC-ZIF-67, and ZIF-67 film all exhibit similar type I isotherms, with high nitrogen adsorption capacity at low relative pressures.[37] This indicates that they share similar micro-porous structures, and the corresponding micro-pore size distribution curve also validates this point (Figure 3f). The Brunauer–Emmett–Teller (BET) surface area and micro-pore volume of OMMF-ZIF-67 are 1345 $m^2\ g^{-1}$ and 0.74 $cm^3\ g^{-1}$, slightly lower than those of MMC-ZIF-67 (1564 $m^2\ g^{-1}$ and 0.82 $cm^3\ g^{-1}$), and higher than those of ZIF-67 film (407 $m^2\ g^{-1}$ and 0.49 $cm^3\ g^{-1}$). Furthermore, Figures 1e and 3a illustrate the presence of macro-pores in OMMF-ZIF-67, which greatly increases the specific surface area of the sample and does not affect the inherent micro-porous structure of ZIF-67. Specifically, the abundant micro-porous structure in OMMF-ZIF-67 ensures the exposure of active sites, while the designed macro-porous structure provides sufficient channels to facilitate the diffusion of biomolecules within the structure, thereby ensuring fast mass transfer and efficient electrochemical sensing of target biomolecules.

Non-invasive blood glucose monitoring represents an appealing alternatives for finger pricks, facilitating glucose assessment and diabetes management.[38] Numerous studies indicated that the sweat glucose concentration correlates closely with the blood glucose concentration.[29] Consequently, a precise, sensitive, and convenient wearable epidermal sweat glucose sensor presents substantial potential for widespread applications.[39] Based on our prior research, ZIF-67 film exhibited robust sensing performance for sweat glucose.[40] Nevertheless, ZIF-67 film is compact, featuring only micro-scopic crystalline pores, which poses a challenge on swift passage of electrolytes and biomolecules.[41] The current OMMF-ZIF-67 offers a viable solution to address the issues mentioned above. A comprehensive examination was carried out on the sensing performance of OMMF-ZIF-67 toward glucose, as well as comparative MMC-ZIF-67 and ZIF-67 film. Initially, to quantitatively investigate the electrochemical activity of OMMF-ZIF-67, we evaluate the active region by using $K_3[Fe(CN)_6]$ as a probe. As illustrated in **Figure 4a**, cyclic voltammetry (CV) scans of OMMF-ZIF-67 at different rates for 5 mM $K_3[Fe(CN)_6]$ could distinctly show oxidation and reduction peaks, and the peak currents of oxidation and reduction linearly increase as the CV scanning rate escalated from 20 to 120 mV s^{-1}. The active area (S_A) of the electrode can be calculated according to the Randles-Sevcik equation:[42] $I_{peak} = (2.69 \times 10^5)n^{3/2}S_A D^{1/2}Cv^{1/2}$, where n is the number of transferred electrons (1 in present instance), D is the diffusion coefficient of $K_3[Fe(CN)_6]$ (6.5×10^{-6} $cm^2\ S^{-1}$ in 0.1 M PBS solution), and C is the total concentration of $K_3[Fe(CN)_6]$ (5 mM in present instance). According to the fitting result of the peak current versus the square root of the scanning rate in the inset of Figure 4a, the active area S_A of OMMF-ZIF-67 is calculated to be 0.179 cm^2, and this is attributed to the macro-pores fabricated by the template method and the abundant micro-pores of the ZIF-67 itself.[43]

CV scan is also utilized to explore the sensing performance of OMMF-ZIF-67. Figure S14 (Supporting Information) illustrates the CV scans conducted at a scan rate of 30 mV s^{-1} within a potential range of −0.1–0.7 V for the OMMF-ZIF-67 electrode, with and without 1 mM glucose in the electrolyte. The CV results reveal two reduction peaks at ~0.46 and ~0.05 V, and a broad oxidation peak at ~0.28 V, which is related to the redox behavior of ZIF-67 in alkaline conditions. Notably, the presence of glucose significantly enhances the current response of the oxidation and reduction peaks, indicating that the OMMF-ZIF-67 can catalyze the oxidation of glucose to generate additional current. The electrochemical sensing properties of the electrodes is further assessed through current-time (i-t) testing. Figure S15 (Supporting Information) illustrates the influence of applied potential on the current response of OMMF-ZIF-67 in 0.1 M PBS containing 1 mM glucose. The results indicate that at 0.6 V, OMMF-ZIF-67 exhibits a significant current response. Hence, the non-enzymatic sensing performance of OMMF-ZIF-67 for glucose is then quantitatively evaluated at a voltage of 0.6 V. Moreover, we also notice that the thickness of the OMMF-ZIF-67 has an impact on its sensing performance, as shown in Figure S16 (Supporting Information). Thinner film displays inferior performance due to fewer active sites, while overly thick MOF film leads to poor conductivity for ion transport, thereby reducing the sensing performance. By adjusting the thickness of the PS template, the ≈100 µm thick OMMF-ZIF-67 exhibits relatively superior sensing performance and will be used in the following studies. On the other hand, the size of the macro-pores can hardly affect the sensing performance (Figure S17, Supporting Information). In addition, Figure S18 (Supporting Information) presents the response current of the ALD ZnO nanomembane toward 100 µM glucose, and it is noted that the current response is much smaller compared to ZIF-67-based samples. This rules out the contribution of residual ZnO on the sensing performance of the OMMF-ZIF-67.

Figure 4b displays the i-t curves of OMMF-ZIF-67 as well as MMC-ZIF-67 and ZIF-67 film are used for comparison with the sequential addition of different concentrations of glucose at 0.6 V in 0.1 M PBS. With addition of glucose, all three samples exhibit notable current responses, indicating that ZIF-67 crystals possess excellent non-enzymatic catalytic sensing capabilities

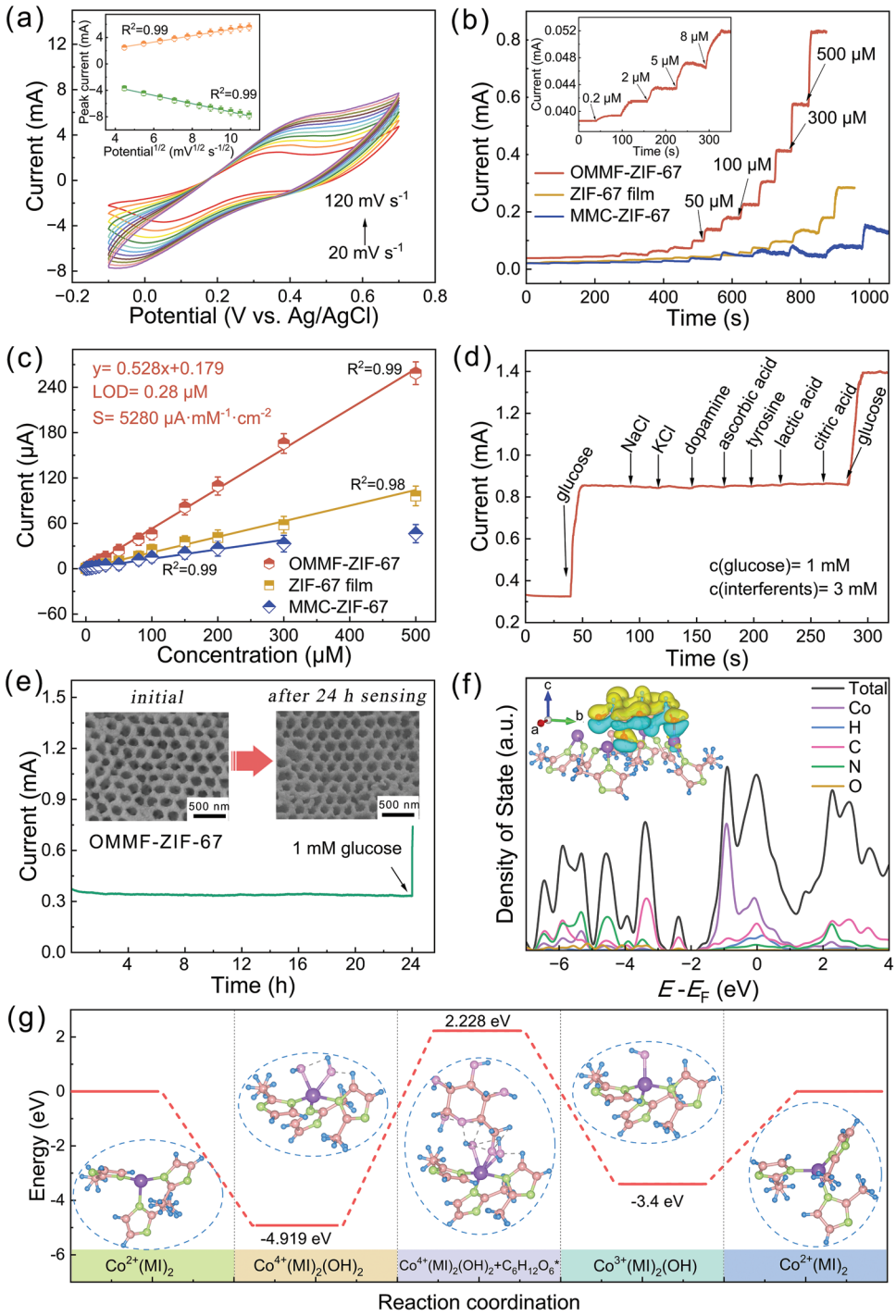

Figure 4. a) CV scans of OMMF-ZIF-67 in 0.1 M PBS containing 5 mM $K_3[Fe(CN)_6]$ at various scan rates of 20–120 mV s^{-1}. The inset shows the fitted curves of oxidation and reduction peak currents as a function of the square root of the scan rate. b) i-t curves of OMMF-ZIF-67, MMC-ZIF-67, and ZIF-67 film upon successive addition of glucose with varying concentrations in 0.1 M PBS at 0.6 V. c) Fitting curves of current response of OMMF-ZIF-67, MMC-ZIF-67, and ZIF-67 film, derived from (b). d) i-t curve of OMMF-ZIF-67 upon sequential addition of 1 mM glucose, 3 mM NaCl, 3 mM KCl, 3 mM dopamine, 3 mM ascorbic acid, 3 mM tyrosine, 3 mM lactic acid, 3 mM citric acid, and 1 mM glucose in 0.1 M PBS at 0.6 V. e) i-t curve of OMMF-ZIF-67 in 0.1 M PBS with 1 mM glucose at 0.6 V. 1 mM glucose was added to the solution after 24 h to test for property recovery. The inset displays the FESEM images of OMMF-ZIF-67 before and after 24 h of continuous sensing testing. f) DOS of the ZIF-67 after adsorbing glucose molecule. Inset is the differential charge density of glucose molecule adsorbed on ZIF-67. g) Free energy diagrams for catalytic sensing reaction of the glucose molecule on ZIF-67. The inset shows the corresponding model for DFT calculation.

for glucose. Moreover, compared with MMC-ZIF-67 and ZIF-67 film, OMMF-ZIF-67 distinctly demonstrates a stronger current response and faster sensing speed. The calibration plots of the current responses to glucose are shown in Figure 4c. OMMF-ZIF-67 exhibits an ultrahigh sensitivity of 5280 μA mM^{-1} cm^{-2} and a linear range of 0.5–500 μM (linear regression equation: Y = 0.528X + 0.179, correlation coefficient $R^2 = 0.99$). In comparison, MMC-ZIF-67 and ZIF-67 film exhibit relatively low sensitivities of 2070 and 1250 μA mM^{-1} cm^{-2}, respectively. Moreover, a nonlinear relationship at high concentration is seen in MMC-ZIF-67 and comes with a large margin of error. In addition, according to the equation: limit of detection (LOD) = $3\delta/S$, where δ represents standard deviation and S is the sensitivity,[44] the LOD of OMMF-ZIF-67 is calculated to be 0.28 μM, whereas it is 0.71 and 1.18 μM for the MMC-ZIF-67 and ZIF-67 film, respectively. Table S1 (Supporting Information) presents a detailed comparison of the performance of current glucose sensors with other MOF-based glucose sensors reported in the literature, which confirms the impressively high performance of OMMF-ZIF-67 electrode.

Further evaluation of the sensing performance is essential and therefore was carried out in our work. Figure 4d demonstrates the i-t curve of OMMF-ZIF-67 with sequential addition of 1 mM glucose, 3 mM NaCl, 3 mM KCl, 3 mM dopamine, 3 mM ascorbic acid, 3 mM tyrosine, 3 mM lactic acid, 3 mM citric acid, and 1 mM glucose at 0.6 V in 0.1 M PBS. The results indicate that the current responses generated by these sweat interference substances are negligible compared to the glucose response, demonstrating the excellent selective sensing capability of OMMF-ZIF-67. In addition, when 1 mM glucose is detected again after the addition of seven biomolecules, the response remains unchanged, exhibiting a stable sensing ability and a robust resistance to interference. The long-term stability of OMMF-ZIF-67 is further explored in 0.1 M PBS containing 1 mM glucose. As shown in Figure 4e, OMMF-ZIF-67 exhibits a steady current response within 24 h without significant attenuation. After 24 h of detection, the sensor still exhibits a significant current response when exposed to 1 mM glucose. Correspondingly, the inset of Figure 4e displays the FESEM images of OMMF-ZIF-67 before and after 24 h of sensing testing. It is observed that 24 h catalytic reaction only caused minor morphological changes in the film, while the overall continuous macro-porous film structure remains stable. This indicates that the sensor possesses good long-term stability, while the slight morphological variation may be attributed to the change in the compactness of the crystal arrangement due to the influence of the liquid.[45] Moreover, in Figure S19 (Supporting Information), the high-resolution Co 2p XPS spectrum after glucose sensing testing shows that there is no significant peak shift compared to the pre-detection spectrum, further confirming that the crystal structure of OMMF-ZIF-67 remain unchanged after 24 h sensing test. In current work, the short-term repeatability of OMMF-ZIF-67 is evaluated by repeatedly detecting 1 mM glucose by using the same sensor for seven times. The statistics in Figure S20a (Supporting Information) indicate similar current responses, with a relative standard deviation (RSD) of 2.35%, elucidating excellent repeatability of the sensor. Six different sensing electrodes are also used to measure the response currents toward 1 mM glucose (three times for each electrode), and the small deviation of the response current (RSD = 3.44%) indicates that OMMF-ZIF-67 has good reproducibility (Figure S20b, Supporting Information). We propose that the excellent sensing performance of OMMF-ZIF-67 compared to MMC-ZIF-67 and ZIF-67 film can be attributed to its deliberately engineered hierarchically macro-micro-porous structure. First, the ordered continuous macro-porous structure enables superior substance transport to all accessible active sites. Second, the continuous MOF film provides a stable conductive pathway for ion transfer. Furthermore, the uniform film ensures adequate exposure of active sites, significantly enhancing catalytic performance.

To thoroughly understand the sensing mechanism of OMMF-ZIF-67 for glucose, we also conducted theoretical simulation. The nonenzymatic sensing of glucose involves two steps: glucose molecule adsorption activation and catalytic reaction to generate an electric current signal.[46] Here, the adsorption mechanism of glucose on ZIF-67 is investigated based on density functional theory (DFT) and the optimized OMMF-ZIF-67 structural model is illustrated in Figure S21 (Supporting Information). The calculated density of state (DOS) after adsorption of glucose molecule (Figure 4f), compared with the DOS of bare OMMF-ZIF-67 (Figure S22, Supporting Information), reveals two new peaks at ~−2.4 and ~−3.3 eV, which are associated with the chemical bonds related to O and H.[47] In previous literature, the low energy peak may be attributed to hydrogen bonding, while the high energy peak may result from the activated O—H covalent bond in glucose.[48] Therefore, the DOS results indicate that the adsorption of glucose is enhanced due to the role of hydrogen bonding. Differential charge density calculations are also utilized to further validate the adsorption performance. The blue color in the differential charge density distribution of Figure 4f represents electron loss, yellow represents electron gain, and the size of the electronic cloud represents the range and intensity of charge transfer. In the case of binding glucose, the larger electronic cloud and charge transfer range indicate a higher absolute value of molecular adsorption energy.[49] The sensing mechanism of OMMF-ZIF-67 for activated glucose may be based on the following equations:[50]

$$\left[Co^{2+}(MI)_2\right]_n + 2nOH^- \rightarrow \left[Co^{4+}(MI)_2(OH)_2\right]_n + 2ne^- \quad (1)$$

$$2\left[Co^{4+}(MI)_2(OH)_2\right]_n + nC_6H_{12}O_6 \rightarrow 2\left[Co^{3+}(MI)_2(OH)\right]_n + nC_6H_{10}O_6 + 2nH_2O \quad (2)$$

$$\left[Co^{3+}(MI)_2(OH)\right]_n + ne^- \rightarrow \left[Co^{2+}(MI)_2\right]_n + nH_2O \quad (3)$$

Figure 4g illustrates the free energy diagram corresponding to each step of the reaction and the models used for DFT calculations. The process of ZIF-67 (Co^{2+}) catalyzing the conversion of glucose into ZIF-67 (Co^{3+}) releases a considerable amount of free energy of up to 3.4 eV, indicating the ease of occurrence of the catalytic reaction. The strong adsorption and high catalytic performance of OMMF-ZIF-67 for glucose molecules enable the molecules that contact the active sites to be rapidly catalyzed and converted to produce the corresponding response current.

3. Conclusion

In summary, we developed a general strategy for constructing MOF film with hierarchically porous structure with the assistance of ALD. Specifically, the MOF crystals grow within the empty space of ordered PS template with the assistance of ALD ZnO nanomembrane due to its induction effect. Upon template removal, an continuous MOF film with ordered macro-micro-porous structure is formed. In this strategy, the MOF species and macro-pores can be modulated on demand, and this macro-micro-porous film demonstrates potential in electrochemical applications. For example, compared to MMC-ZIF-67 and ZIF-67 film, the obtained OMMF-ZIF-67 exhibits an ultrahigh sensitivity of 5280 μA mM^{-1} cm^{-2} and a low LOD of 0.28 μM toward glucose due to enhanced mass transfer, large active sites exposure, and stable electronic conduction network. The corresponding epidermal sweat glucose sensing device fabricated by transfer process also exhibits high sensing properties. We believe that such OMMF-MOF can open up new windows of future applications in, e.g., sensing diffusion control, catalytic cascade reactions, and on-chip integrated devices.

4. Experimental Section

Materials: Cobalt nitrate hexahydrate ($Co(NO_3)_2{\cdot}6H_2O$), dimethylimidazole (2-MI), D(+)-glucose monohydrate (AR, ≥99.7%), potassium ferricyanide ($K_3[Fe(CN)_6]$, AR, ≥99.5%), polyvinylpyrrolidone K30 (PVP, ≥99.7%), potassium persulfate ($K_2S_2O_8$, ≥99.7%), hydrochloride dopamine (≥97%), NaCl (AR, ≥99.7%), KCl (AR, ≥99.7%) and lactic acid (AR, ≥99.7%) were sourced from Sinopharm Chemical Reagent Co. Ltd. Methanol (AR, ≥99.5%), NaOH (AR, ≥99.7%), N,N-dimethylformamide (DMF, AR, ≥99.5%), styrene (≥99.7%) and ethanol (AR, ≥99.7%) were purchased from Shanghai Aladdin Biochemical Technology Co., Ltd. PEDOT/PSS (1.3 wt.% dispersion in H_2O) and graphite paper were procured from Sigma-Aldrich. Solutions for electrochemical activity measurements were prepared using 0.1 M PBS (pH 7.2), unless otherwise specified. All experiments utilized deionized water purified through a Millipore system. All reagents were used as received without further purification.

Preparation of 3D Ordered PS Template: Four different sizes (≈150, ≈200, and ≈260 nm) of monodisperse colloidal PS were synthesized following a reported procedure with some modifications. In the typical synthesis of ≈200 nm PS, 32.5 mL washed styrene (stabilizer removed by 20 mL 10 wt.% NaOH) was added to a 500 mL three-necked flask containing 250 mL water and 0.5 g PVP. After bubbling with nitrogen for 15 min, the mixture was then allowed to flow under magnetic stirring at 90 °C for 30 min. Subsequently, 10 mL water solution containing 0.1 g $K_2S_2O_8$ was added to the flask to initiate the polymerization reaction of styrene. After stirring at 300 rpm for 24 h, monodisperse colloidal PS was obtained. The monodisperse PS was centrifuged at a rate of 5k rpm for 10 min, dried at 60 °C, and finally prepared into a 3D ordered PS template.

Deposition of ZnO Nanomembrane on PS Template via ALD: ZnO nanomembrane was deposited on the 3D ordered PS template via ALD of 300 cycles. In a laboratory-built ALD system, the deposition of ZnO nanomembrane was conducted at a relatively low temperature (60 °C). Diethylzinc (DEZ) and DI water were used as the deposition precursors. To ensure uniform deposition of ZnO nanomembrane on the gaps of the 3D ordered PS template, the pulse waiting time was extended to 10 s. A typical ALD cycle includes DEZ pulse (30 ms), waiting time (10 s), N_2 purge (30 s), DI water pulse (35 ms), waiting time (10 s), and N_2 purge (30 s).

Preparation of OMMF-ZIF-67: Initially, $Co(NO_3)_2{\cdot}6H_2O$ (1.45 g) was dissolved in a mixture of methanol (40 mL) and ethanol (40 mL) to form solution A. 2-MI (1.65 g) was dissolved in the same mixture of methanol (40 mL) and ethanol (40 mL) to form solution B. The ALD ZnO-coated PS template was then placed into the beaker containing solution A. Subsequently, the solution was transferred into a vacuum drying oven for 10 min of vacuum degassing to ensure that all PS voids were filled with solution A. The beaker was then sealed at 60 °C for 24 h. Upon cooling to room temperature, solution B was added dropwise, and the beaker was vacuum degassed again for 10 min. The mixture was further aged at room temperature for 24 h. Subsequently, the sample was taken out, washed with ethanol, and dried at 50 °C for 2 h. Next, the sample was immersed in DMF for 30 min to dissolve and remove the PS template, and DMF is washed off with dichloromethane. The obtained OMMF-ZIF-67 exhibits a free-standing state. Finally, OMMF-ZIF-67 was dried in a critical point dryer (Leica CPD030) to preserve the macro-micro-porous film structure.

Synthesis of MMC-ZIF-67: MMC-ZIF-67 were also synthesized for structural and performance comparison. Initially, a saturated methanol solution C containing $Co(NO_3)_2{\cdot}6H_2O$ (0.5 g mL^{-1}) and 2-MI (1.25 g mL^{-1}) was prepared. The 3D ordered PS template was then immersed into the prepared solution C and degassed for 10 min to ensure that all gaps between the 3D colloidal spheres were filled with the precursor solution. The samples were then dried at 50 °C for 12 h. Next, the sample was immersed into a 30 mL $CH_3OH/NH_3{\cdot}H_2O$ (1:1 v/v) mixed solution and vacuum degassed for 10 min. After 24 h of immersion, the obtained sample was taken out and dried at 50 °C for 12 h. Lastly, the sample was washed first by using DMF to remove the PS template, and then by using dichloromethane to clear DMF. The MMC-ZIF-67 was finally dried at 50 °C for 12 h.

Synthesis of ZIF-67 Film: A uniform PEDOT/PSS layer (sacrificial layer) with a thickness of ≈10 μm was spin-coated on a glass slide substrate, and cured at 90 °C for 12 h. Afterward, the substrate with the sacrificial layer was deposited with 300 cycles of ZnO nanomembrane according to the above-mentioned ALD process. The ALD ZnO nanomembrane-coated substrate was then placed into a beaker containing solution A. The beaker was sealed at 60 °C for 24 h. Upon cooling to room temperature, solution B was added dropwise, and the mixture was further aged at room temperature for 24 h. Subsequently, the substrate was taken out, washed with ethanol, and the PEDOT/PSS as the sacrificial layer was dissolved with DI water to obtain a free-standing MOF film.

Preparation of the Epidermal Sweat Sensing Device: The PDMS substrate was formed by spin-coating a mixture of prepolymer and curing agent in the ratio of 10:1 and cut into a rectangle of 1 cm × 1 cm. A uniform photoresist (ARP-3510, Allresist GmbH) layer, ≈2 μm thick, was spun onto the surface of the substrate. Then, the photoresist layer was patterned to the intended design through UV lithography (SUSS MA6). Subsequently, a 10 nm Ge film and a 50 nm Au film were deposited by magnetron sputtering. Next, the photoresist layer was removed with acetone, cleaned with ethanol, and deionized water to obtain the patterned Ge/Au electrode. The OMMF-ZIF-67 and Ag/AgCl paste were transferred to specific regions of the electrode pattern. Finally, aluminum wire was spot-welded at the pins to form the epidermal sweat sensing device.

Structural Characterizations: The morphology of all samples was characterized using a FESEM (Sigma 300, ZEISS). The composition of the samples was analyzed using EDX (Oxford Xplore 30). XRD patterns of films and particles were obtained on an X'Pert Pro X-ray diffractometer equipped with Cu Kα radiation ($\lambda = 0.1542$ nm) at 40 kV and 40 mA. XPS analysis of the samples was conducted using a Thermo Scientific Nexs instrument, and the spectra were curve-fitted using XPS Peak 4.0 software. TGA testing was performed using a METTLER TGA2 instrument in air atmosphere at a heating rate of 10 °C min^{-1}. Nitrogen adsorption/desorption measurements were carried out at 100 °C for 12 h on a Micromeritics ASAP 2460 surface area and porosity analyzer. The specific surface area was calculated using the single point Brunauer–Emmett–Teller (BET) method. Pore size distribution was calculated from nitrogen adsorption data using the Barrett Joyner–Halenda (BJH) method. The macro-pore distribution was measured by mercury intrusion porosimetry (AutoPore 9510, Micromeritics Instrument Corporation).

Electrochemical Characteristics: The electrochemical glucose sensing tests were evaluated on a CHI660E (Chenhua Instrument, Shanghai, China) electrochemical workstation with a three-electrode configuration. In this experiment, Ag/AgCl (in saturated KCl solution) served as the reference electrode, a graphite rod was used as the counter electrode. The

free-standing OMMF-ZIF-67 was transferred onto a graphite paper and adhered by using Nafion as the working electrode. For performance comparison, several additional electrodes were prepared: ZIF-67 film was transferred onto a graphite paper; ZnO nanomembrane was directly deposited on graphite paper via ALD; and MMC-ZIF-67 was attached to a glass carbon (GC, diameter: 3 mm). Specifically, to prepare the MMC-ZIF-67 electrode, a mixed sol of MMC-ZIF-67 with ethanol and Nafion (5 wt.%) was prepared and the sol was then dropped onto the GC electrode and dried.

In Vitro Biocompatibility Assay: The culture medium used in the experiment was α-MEM media (Gibco, Invitrogen Inc), supplemented with 10% fetal bovine serum (FBS, USA), 1% antimicrobial penicillin, and streptomycin (USA). In order to check the biocompatibility of the OMMF-ZIF-67, OMMF-ZIF-67 extract was prepared by immersing OMMF-ZIF-67 in 1 mL of blank culture medium for 24 h, and then filtering the culture medium with a sterile 0.22 µm filter head. Human dermal fibroblasts provided by Cell Bank, Chinese Academy of Sciences, were cultured at 37 °C in an incubator (5% CO_2 and 95% relative humidity). Specifically, human dermal fibroblasts (5×10^3 cells well^{-1}, 100 µL) were inoculated with blank culture medium in 96-well plates for 6 h. Afterward, the culture medium was replaced with an equal amount of extract. The incubation was continued in the medium for 24 and 48 h and then 120 µL of medium containing 10% alamarBlue (Invitrogen, USA) was added to each well for additional incubation of 2 h. The fluorescence intensity was detected by a Microplate Reader (Cytation 5, BioTek, USA) with excitation wavelength of 560 nm and emission wavelength of 590 nm. Cell viability was assessed by using a live/dead cell staining kit (Biovision, USA). Specifically, human dermal fibroblasts (5.0×10^3 cells mL^{-1}) were cultured with OMMF-ZIF-67 extract for two days. Then, 100 µL fresh PBS with calcein-AM and propidium iodide was introduced for another 30-min incubation. Finally, fluorescent photograph was obtained by using a fluorescence microscope (Olympus, Japan). For biocompatibility assessment, human dermal fibroblasts were also cultured with just blank culture medium in the experiment while other processes are the same.

Supporting Information

Supporting Information is available from the Wiley Online Library or from the author.

Acknowledgements

This work was supported by the National Key Technologies R&D Program of China (2021YFA0715302), the National Natural Science Foundation of China (52203328 and 62375054), the Science and Technology Commission of Shanghai Municipality (22ZR1405000, 24520750200, and 24CL2900200), Shanghai Talent Programs, the Fundamental Research Funds for the Central Universities (2232023A-10), and the Major/ key program of State Key Laboratory for Modification of Chemical Fibers and Polymer Materials (23M1060280).

Conflict of Interest

The authors declare no conflict of interest.

Author Contributions

J.L.W. and Y.Y.J. contributed equally to this work. The manuscript was written through contributions of all authors. All authors have given approval to the final version of the manuscript.

Data Availability Statement

The data that support the findings of this study are available from the corresponding author upon reasonable request.

Keywords

atomic layer deposition, biosensor device, induced assembly, macro-micro-porous, metal-organic framework film

Received: October 18, 2024
Revised: January 4, 2025
Published online:

[1] W. J. Wang, K. Z. Su, D. Q. Yuan, *Mater. Chem. Front.* **2023**, *7*, 5247.
[2] Y. Q. Luo, Y. X. Mei, Y. Xu, K. Huang, *Nanomaterials.* **2023**, *13*, 2514.
[3] S. J. Liu, X. X. He, X. Hu, Y. Y. Pu, X. Mao, *Mater. Adv.* **2024**, *5*, 453.
[4] Y. Q. Zhu, X. H. Wang, M. X. Wu, *Adv. Funct. Mater.* **2023**, *33*, 2308096.
[5] E. Jo, S. H. Yang, D. W. Kim, D. W. Kang, *Coord. Chem. Rev.* **2024**, *515*, 215958.
[6] J. Ferrando-Soria, A. Fernandez, *Nano-Micro Lett.* **2024**, *16*, 88.
[7] A. Sharma, S. B. Eadi, H. Noothalapati, M. Otyepka, H. D. Lee, K. Jayaramulu, *Chem. Soc. Rev.* **2024**, *53*, 2530.
[8] X. J. Wu, X. D. Yu, Z. K. Zhang, H. Y. Liu, S. D. Ling, X. Y. Liu, C. Lian, J. H. Xu, *Adv. Funct. Mater.* **2023**, *33*, 2300329.
[9] Y. Q. Li, Z. H. Wei, Z. H. Zhan, J. J. Pei, C. F. Zhao, W. Q. Xu, Q. Sun, W. X. Chen, S. H. Li, S. P. Pang, *J. Energy Storage.* **2024**, *76*, 109778.
[10] J. Wang, Y. Ren, W. Li, L. M. Wu, Y. H. Deng, *Small Methods.* **2023**, *7*, 2201687.
[11] L. B. Sun, J. R. Li, J. Park, H. C. Zhou, *J. Am. Chem. Soc.* **2012**, *134*, 126.
[12] G. R. Cai, H. L. Jiang, *Angew. Chem., Int. Ed.* **2017**, *56*, 563.
[13] S. Han, M. S. Lah, *Cryst. Growth Des.* **2015**, *15*, 5568.
[14] T. Sun, S. Zhao, W. Chen, D. Zhai, J. Dong, Y. Wang, S. Zhang, A. Han, L. Gu, R. Yu, X. Wen, H. Ren, L. Xu, C. Chen, Q. Peng, D. Wang, Y. Li, *Proc. Natl. Acad. Sci. U. S. A.* **2018**, *115*, 12692.
[15] C. Wang, H. Y. Zhang, Y. Wang, J. Wu, K. O. Kirlikovali, P. Li, Y. M. Zhou, O. K. Farha, *Small.* **2023**, *19*, 2206116.
[16] W. Yao, A. Q. Hu, J. T. Ding, N. S. Wang, Z. Qin, X. F. Yang, K. Shen, L. Y. Chen, Y. W. Li, *Adv. Mater.* **2023**, *35*, 2301894.
[17] K. Shen, L. Zhang, X. D. Chen, L. M. Liu, D. L. Zhang, Y. Han, J. Y. Chen, J. L. Long, R. Luque, Y. W. Li, B. L. Chen, *Science.* **2018**, *359*, 206.
[18] F. L. Wang, T. T. Hou, X. Zhao, W. Yao, R. Q. Fang, K. Shen, Y. W. Li, *Adv. Mater.* **2021**, *33*, 2102690.
[19] H. Hong, J. L. Liu, H. W. Huang, C. A. Etogo, X. F. Yang, B. Y. Guan, L. Zhang, *J. Am. Chem. Soc.* **2019**, *141*, 14764.
[20] W. Li, J. Liu, P. F. Guo, H. Z. Li, B. Fei, Y. H. Guo, H. G. Pan, D. L. Sun, F. Fang, R. B. Wu, *Adv. Energy Mater.* **2021**, *11*, 2102134.
[21] R. Haldar, C. Wöll, *Nano Res.* **2021**, *14*, 355.
[22] J. Zheng, L. Y. Chen, Y. X. Kuang, G. F. Ouyang, *Small.* **2024**, *20*, 2307976.
[23] I. E. Khalil, J. Fonseca, M. R. Reithofer, T. Eder, J. M. Chin, *Coord. Chem. Rev.* **2023**, *481*, 215043.
[24] C. Liu, Q. Sun, L. Lin, J. Wang, C. Q. Zhang, C. H. Xia, T. Bao, J. J. Wan, R. Huang, J. Zou, C. Z. Yu, *Nat. Commun.* **2020**, *11*, 4971.
[25] Y. Wang, L. Jin, S. Y. Hua, Z. Zhao, Z. J. Xiao, C. Y. Qu, J. Y. Huang, G. S. Huang, X. Y. Ke, Z. H. Lu, J. Tan, X. Y. Liu, Y. F. Mei, *J. Materiomics.* **2023**, *9*, 1113.
[26] Z. C. Zhou, L. N. Xu, Y. H. Ding, H. P. Xiao, Q. Shi, X. H. Li, A. D. Li, G. Y. Fang, *Prog. Mater. Sci.* **2023**, *138*, 101159.
[27] Z. Zhang, Y. W. Liu, H. R. Tian, X. J. Ma, Q. Yue, Z. X. Sun, Y. Lu, S. X. Liu, *ACS Nano.* **2021**, *15*, 16581.
[28] B. M. Wu, Z. Y. Zhang, B. X. Chen, Z. Zheng, C. Y. You, C. Liu, X. Li, J. L. Wang, Y. Q. Wang, E. M. Song, J. Z. Cui, Z. H. An, G. S. Huang, Y. F. Mei, *Sci. Adv.* **2023**, *9*, eadi7805.

[29] Z. Zhao, Y. Kong, X. Y. Lin, C. Liu, J. R. Liu, Y. Y. He, L. L. Yang, G. S. Huang, Y. F. Mei, *J. Mater. Chem. A.* **2020**, *8*, 26119.
[30] T. Zorlu, D. Hetey, M. R. Reithofer, J. M. Chin, *Acc. Chem. Res.* **2024**, *57*, 2105.
[31] H. M. Albetran, *Materials.* **2023**, *16*, 1749.
[32] S. S. Fouad, M. Nabil, B. Parditka, A. M. Ismail, E. Baradács, H. E. Atyia, Z. Erdélyi, *J. Nanopart. Res.* **2023**, *25*, 172.
[33] S. P. Zhang, J. Ding, D. Y. Tian, W. H. Su, J. Y. Zhu, X. L. Ma, M. H. Lu, *J. Solid State Chem.* **2024**, *336*, 124769.
[34] Z. L. Wang, X. Zhou, K. Zheng, Y. Guo, J. Wang, W. B. Liu, H. Zhou, T. Zhao, *Compos. Part A.* **2023**, *174*, 107740.
[35] Y. B. Li, Z. L. Jin, T. S. Zhao, *Chem. Eng. J.* **2020**, *382*, 123051.
[36] W. Zhang, X. F. Jiang, X. B. Wang, Y. V. Kaneti, Y. X. Chen, J. Liu, J. S. Jiang, Y. Yamauchi, M. Hu, *Angew. Chem.* **2017**, *56*, 8435.
[37] X. C. Huang, Y. Y. Lin, J. P. Zhang, X. M. Chen, *Angew. Chem., Int. Ed.* **2006**, *45*, 1557.
[38] L. J. Shang, S. Q. Yu, X. W. Shang, X. Y. Wei, H. Y. Wang, W. S. Jiang, Q. Q. Ren, *J. Appl. Electrochem.* **2024**, *54*, 1807.
[39] X. S. Huang, C. J. Yao, S. Huang, S. T. Zheng, Z. J. Liu, J. Liu, J. Wang, H. J. Chen, X. Xie, *ACS Sens.* **2024**, *9*, 1065.
[40] Z. Zhao, X. Y. Ke, J. Y. Huang, Z. Y. Zhang, Y. Wu, G. S. Huang, J. Tan, X. Y. Liu, Y. F. Mei, J. H. Chu, *Adv. Sci.* **2024**, *11*, 2310189.
[41] Z. Y. Li, Z. W. Li, N. Zhang, J. J. Bao, X. P. Zhang, G. H. He, C. Chen, Y. C. Song, *J. Membr. Sci.* **2024**, *694*, 122428.
[42] A. Nisar, M. A. Khan, Z. Hussain, *J. Korean Ceram. Soc.* **2022**, *59*, 359.
[43] Y. A. Wang, J. Yan, W. W. Zhu, Y. H. Zhang, K. R. Cao, B. Zhang, X. H. Yu, Q. F. Shen, C. X. Liu, Q. Wang, *Mater. Res. Express.* **2023**, *10*, 025006.
[44] S. J. Kim, H. J. Koh, C. E. Ren, O. Kwon, K. Maleski, S. Y. Cho, B. Anasori, C. K. Kim, Y. K. Choi, J. Kim, Y. Gogotsi, H. T. Jung, *ACS Nano.* **2018**, *12*, 986.
[45] X. Chen, J. J. Dong, K. Chi, L. J. Wang, F. Xiao, S. Wang, Y. Zhao, Y. Q. Liu, *Adv. Funct. Mater.* **2021**, *31*, 2102855.
[46] H. H. Jin, W. H. Zeng, W. Qian, L. Li, P. X. Ji, Z. Y. Li, D. P. He, *Nano Res.* **2024**, *17*, 4737.
[47] V. Fung, G. X. Hu, P. Ganesh, B. G. Sumpter, *Nat. Commun.* **2021**, *12*, 88.
[48] K. K. Naik, A. Gangan, B. Chakraborty, S. K. Nayak, C. S. Rout, *ACS Appl. Mater. Interfaces.* **2017**, *9*, 23894.
[49] M. A. Rojas, J. Amalraj, L. S. Santos, *Polymers.* **2023**, *15*, 3370.
[50] X. R. Chen, D. Lau, G. J. Cao, Y. Tang, C. Wu, *ACS Appl. Mater. Interfaces.* **2019**, *11*, 9374.